

A variable-temperature cavity ring-down spectrometer with application to line shape analysis of CO₂ spectra in the 1600 nm region

Mélanie Ghysels¹ · Qingnan Liu¹ · Adam J. Fleisher¹ · Joseph T. Hodges¹ 

Received: 11 January 2017 / Accepted: 28 February 2017 / Published online: 31 March 2017
© Springer-Verlag Berlin Heidelberg (outside the USA) 2017

Abstract We present a new cavity ring-down spectroscopy system which was developed for variable-temperature absorption measurements (220–290 K) of atmospheric gases. This laser spectrometer was developed in the framework of the NASA Orbiting Carbon Observatory-2 project to improve our understanding of line shape parameters for carbon dioxide and oxygen. The apparatus consists of a monolithic, fixed-mirror ring-down cavity within a temperature-regulated enclosure, which is interrogated by a tunable, single-frequency diode laser. We experimentally characterize and model the dependence of the spectrum detuning axis at each setpoint temperature, and show that absolute frequencies are stable to within 200 kHz over several hours, corresponding to temperature stabilities better than 1 mK. We measure the R16e (30013-0001) ¹²C¹⁶O₂ transition and carry out multi-spectrum analyses using two line profiles incorporating speed-dependent (quadratic approximation) and Dicke narrowing (hard collision assumption) effects. The resulting broadening coefficient and temperature exponent are in excellent agreement (0.05% level) with previous high-resolution Fourier-transform spectroscopy measurements, and the speed dependent broadening parameter is within 3% of the theoretical value.

1 Introduction

Current and planned scientific missions dedicated to monitoring greenhouse gases (GHGs) from both space- and

ground-platforms require increasingly accurate line-by-line spectroscopic parameters over the 220–300 K temperature range. For example, the Orbiting Carbon Observatory-2 (OCO-2) NASA satellite mission [1] has a target relative uncertainty of 0.3% in the retrieval of the column-integrated carbon dioxide (CO₂) molar fraction. NASA has similar measurement goals for CO₂ which are required for the TCCON Project and ASCENDS mission, as well as in the European Space Agency (ESA) MERLIN mission which detects methane (CH₄) in the Earth's atmosphere. All of these measurements require accurate, predictive forward models for the relevant spectrally resolved absorption coefficient over an atmospheric column that traverses the lower troposphere through the upper stratosphere. These spectroscopic models need to be validated over a wide range of pressure, temperature and composition consistent with the conditions of interest.

The cavity-ring down spectroscopy (CRDS) laser-absorption technique was introduced by O'Keefe and Deacon in 1988 using pulsed lasers [2] and is now routinely implemented using myriad custom and commercial spectrometers. The essential aspect of CRDS is to measure the decay rate of a circulating light beam that leaks out of a high-finesse optical resonator (i.e. ring-down cavity) containing a light-absorbing sample. CRDS is now usually implemented with single-frequency, continuous-wave (CW) lasers [3, 4]. These types of lasers have bandwidths that are much less than the cavity mode spacing, thus allowing for single-mode excitation and yielding decay signals that can be modeled by a single exponential function. For this case, the circulating probe beam encompasses a narrow range of optical frequencies centered around one cavity mode, and the sample absorption coefficient equals the change in the decay rate divided by the speed of light. This situation leads to high spectral

✉ Joseph T. Hodges
joseph.hodges@nist.gov

¹ Chemical Sciences Division, National Institute of Standards and Technology, Gaithersburg, MD, USA

resolution (cavity mode spacing divided by the finesse) and low detection limit (relative uncertainty in the measured decay rate divided by the cavity length). Cavities usually are of the order of 1 m in length, with mirror losses ($1 - R$) ranging from 10^{-6} to 10^{-3} and relative uncertainties in the measured decay rate of 0.01–0.1%. As a typical example, assuming a 1-m long cavity, mirror losses of 10^{-4} and a relative uncertainty in the decay rate of 0.01%, an absorption coefficient at the 10^{-10} cm^{-1} level or below can be measured without extremely long averaging times. At room temperature, various CRDS spectrometers have yielded detection limits between 10^{-10} and 10^{-11} cm^{-1} [5–11], while a more limited number of systems have been demonstrated to have detection limits in the 10^{-12} to 10^{-13} cm^{-1} [12, 13] range for long averaging times and/or for high acquisition rate cases.

Notably, the spectral resolution of single-mode CRDS is usually not limited by the short-term cavity linewidth (kHz level or below) that is associated with the cavity finesse. The actual resolution of the CRDS measurement is often limited by temperature-induced changes in the cavity length which displace the cavity resonant frequencies. Alternatively, the resolution is limited by imprecision of wavelength meters or etalons that are used to monitor detuning of the probe laser frequency. To compensate for these limitations, the frequency-stabilized cavity ring-down spectroscopy (FS-CRDS) method was developed in our laboratory [5]. With this approach, the ring-down cavity length is actively stabilized by maintaining resonance with a reference laser that has absolute frequency stability. FS-CRDS has been implemented to yield absorption spectra with resolution and long-term stability at the 10–500 kHz level and has enabled measurements of line shapes with signal-to-noise ratios from 10^3 to more than 10^6 [14–17]. The combination of wide dynamic range, high spectrum fidelity and sensitivity offered by FS-CRDS makes it extremely attractive for high-accuracy measurements of line shape parameters, especially for weakly absorbing samples.

Only a few cavity ring-down spectrometers have been developed to measure low-temperature absorption spectra. These include systems employing phase-shift CRDS [18–22], pulsed-laser CRDS [23] and mode-by-mode CRDS [24]. Because of the large physical scale of these spectrometers, large temperature differences, up to several Kelvin, were typically observed across the cavities employed. None of these studies achieved the accuracies in line parameters which are required for remote sensing applications described above. Nor have prior FS-CRDS measurements provided any low temperature results, because these studies correspond to room-temperature conditions. This lack of high-precision, low-temperature line shape measurement capability motivated the development of the spectrometer discussed here.

In the remainder of this article, we present a new variable-temperature cavity ring-down spectrometer spanning the range 220–290 K, and which is thermally stabilized to provide 100-kHz-level spectrum resolution. This apparatus permits the investigation of the temperature and pressure dependence of line shapes, with a spectral precision (x -axis) and signal-to-noise ratio (y -axis) that is commensurate with previous room-temperature FS-CRDS realizations based on active stabilization of the cavity length. We begin by describing the apparatus, dynamic range and measurement precision (Sect. 2), and characterizing the system frequency stability (Sect. 3). In Sect. 4 we discuss speed-dependent line profiles used for data analysis. In Sect. 5 we present spectra of the (30013-00001) band R16e $^{12}\text{C}^{16}\text{O}_2$ transition acquired over the temperature and pressure range 240–290 K and 5–59 kPa, respectively. Finally, we report multispectrum fits of advanced line profiles to these measured spectra and compare our results to previous studies.

2 Variable-temperature cavity ring-down spectrometer

The custom spectrometer described herein resides at the National Institute of Standards and Technology (NIST) in Gaithersburg, Maryland. The assembly comprises a monolithic, low-thermal-expansion, fixed-mirror, vacuum-compatible ring-down cavity which resides within a cooled, temperature-regulated, cylindrical enclosure. Temperature regulation of the enclosure's inside surface is achieved using a closed-loop refrigeration system unlike the approach taken by previous low-temperature ring-down experiments. As shown below, the present system demonstrates excellent temperature stability and minimal temperature gradients, thus satisfying two important conditions required for accurate measurements of spectroscopic parameters.

2.1 Mechanical configuration

The ring-down cavity cell has a relatively simple design as shown in Fig. 1, consisting of an 80-cm-long, tube, with two high-reflectivity ring-down cavity mirrors that are fixed in place. The cell was formed by axially drilling a solid cylindrical rod (made of invar-36), to yield a tubular geometry with OD and ID of 6.35 and 5 cm, respectively. The internal surface of the invar tube also was polished to mirror-like conditions ($0.1 \mu\text{m}$ root-mean-square surface roughness) to minimize water vapor adsorption/desorption effects.

The first flange on each side (red flange in Fig. 1b) holds a ring-down mirror and is sealed to the invar tube by a Teflon o-ring. These flanges also have a 1° -angled

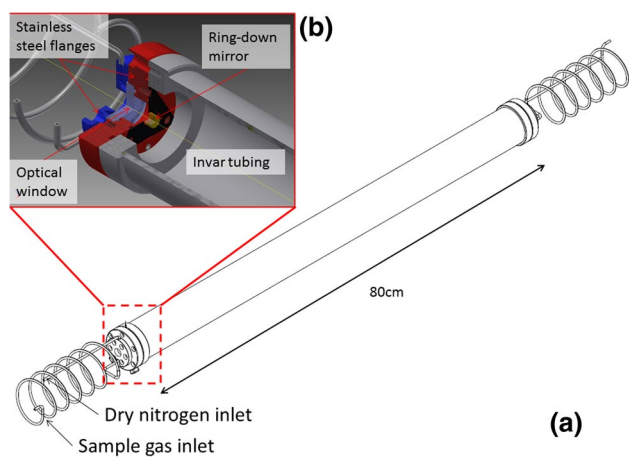


Fig. 1 **a** Diagram of monolithic, invar-36 ring-down cell. **b** Cutaway view of end flange, window and mirror-mount assembly

wedge to reduce Fabry-Pérot etalon effects caused by the windows. On each end, a second flange (blue flange in Fig. 1b, 4.3 cm in diameter) seals the cavity by compressing onto the first flange, which comprises a 2.5-cm diameter stainless-steel adapter holding a 1.27-cm diameter, anti-reflection coated ($\lambda = 1050\text{--}1700$ nm) optical glass window. This sealing arrangement allows the optical cavity to be maintained from vacuum to slightly above atmospheric pressure over the temperature range 240–300 K.

The end faces of the invar tube were machined to be parallel to within 0.2° , because the cavity design did not use any adjustment screws for mirror alignment. This degree of parallelism ensured that the line connecting the centers of curvature of the two high-reflectivity mirrors nearly coincides with the symmetry axis of the tube assembly. Subsequently, the ring-down cavity mirrors were optically aligned with a removable, two-axis mirror mount with the aid of a HeNe laser, and then permanently glued onto a small triangular base mounted onto the first set of flanges (black piece in Fig. 1b). The resulting mirror-to-mirror distance is 80.3 cm. The relative orientation of the mirrors was sufficiently reproducible that the mirror/flange assemblies could be removed and remounted without altering the alignment of the optical resonator.

We note that unlike previous designs of FS-CRDS systems [7], the present system does not have a piezoelectric- (PZT) actuated mirror or bellows assembly. Our other FS-CRDS spectrometers [5] use a PZT to adjust (via a closed-loop servo) the mirror-to-mirror distance, to compensate for thermal expansion and low-frequency vibrations or to scan the cavity mode frequencies. Rather than actively maintaining the cavity length with a PZT-actuated mirror, in the new design, the mirror-to-mirror distance is thermally stabilized by the nearly monolithic,

low-thermal expansion invar-36 assembly and by the temperature stability of the cooling enclosure. The resulting frequency stability of the system (found to be better nominally 200 kHz) is described in Sect. 3.4. Although this fixed-cavity-length approach precludes achieving an arbitrarily high sampling density in the observed spectra, the high precision of the frequency detuning axis allows for measurement of subtle variations in line shape even with a relatively small number of sampled points across each line shape.

The sample gas inlet and outlet lines correspond to a pair of 3-mm OD stainless-steel coils welded onto the first set of flanges. The sample pressure was measured using a resonant Si pressure gauge with a 133 kPa full scale range. This pressure gauge is calibrated against a NIST secondary pressure standard, yielding a maximum relative standard uncertainty less than 0.01% over the range 5 kPa to 133 kPa. The system temperature is measured using a NIST-calibrated $100\ \Omega$ platinum-resistance thermometer (PRT) that is embedded into a hole in one of the stainless-steel end-flanges of the cell. This resistance is measured using an AC bridge with an internal reference resistor. The total temperature measurement uncertainty is dominated by two components: the calibration uncertainty (2.5 mK) and drift in the internal reference resistor of the AC bridge (equivalent to 5 mK). Combining both uncertainties in quadrature gives a total uncertainty of approximately 6 mK for the temperature measurement. There are also two other calibrated PRTs which are read using a data acquisition card: one mounted in the opposite end flange and the other fixed onto the outer surface of the invar tubing midway from each flange. These thermometers are used to quantify thermal gradients along the long axis of the ring-down cell.

2.2 Temperature-regulation system

The invar cell assembly resides within a cylindrical, vacuum-jacketed cooling cell that is temperature-stabilized to ± 5 mK over the range 220–290 K. Fig. 2 shows a schematic of the invar ring-down cell mounted within the cooling enclosure assembly. The actively cooled surface of the enclosure is made of copper, and the invar cell rests on three stainless-steel feet in contact with this copper surface. The feet are welded onto the first set of stainless steel flanges which hold the cavity mirrors.

The cooling system uses a mixture of three refrigerants (28.8% R14, 53.9% R507 and 17.3% R508b by mass) and consists of a closed-loop refrigerator comprising an external controller, electronics, heat-exchanger, compressor and flexible tubing connections to the vacuum-jacketed enclosure containing the ring-down cavity. The three-component mixture allows for a single-stage condenser system,

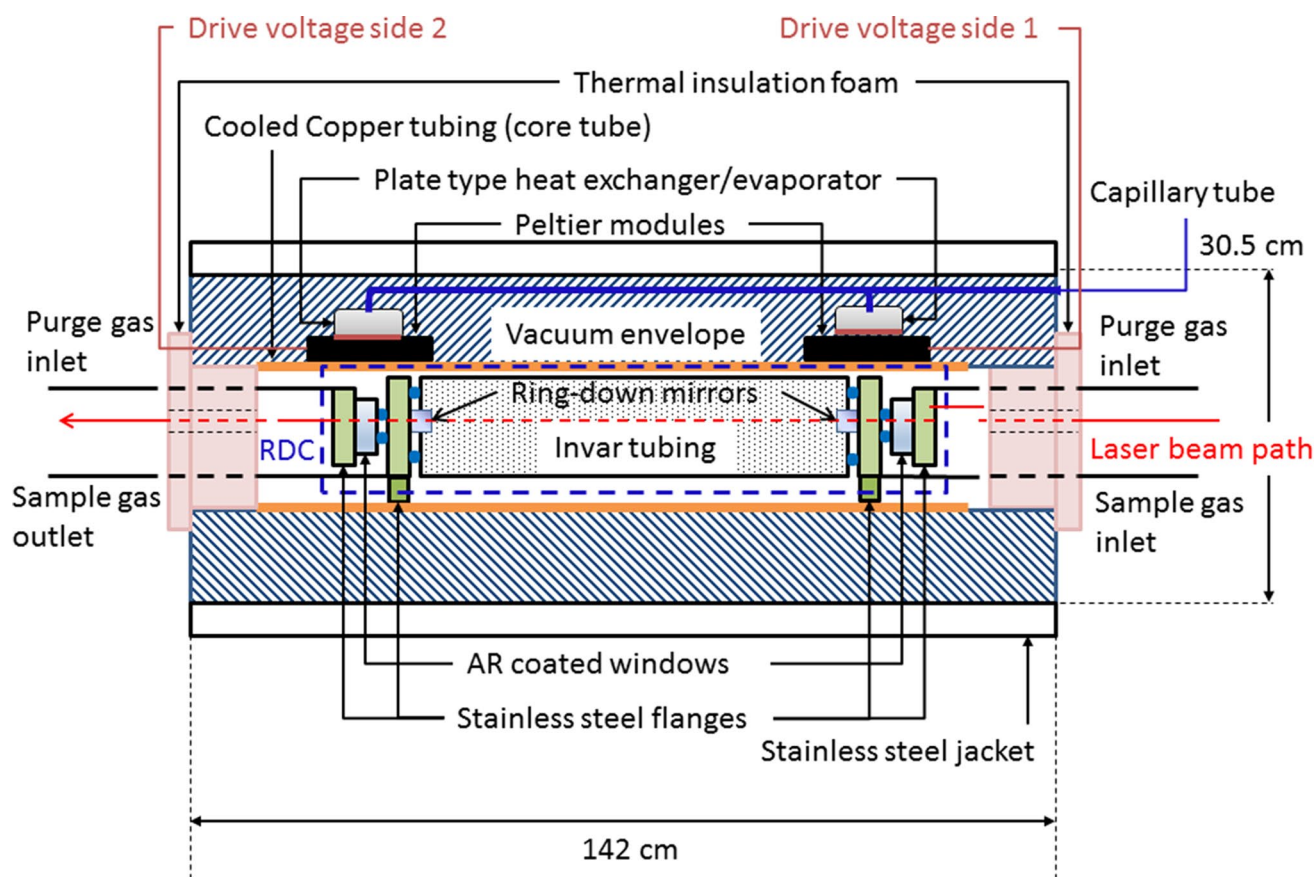


Fig. 2 Schematic of ring-down cell mounted within temperature-regulated enclosure. The vacuum seal is realized by Teflon o-rings (blue circles). Thermal isolation from the surroundings is achieved using insulating foam plugs located at each end of the core copper tubing (pink blocks) and a vacuum envelope which surrounds the cell

(striped pattern). Gaseous samples are introduced through the sample gas inlet and outlet. A separate stream of purge gas cleans the exterior surface of the optical windows and prevents the formation of dew or ice

because the refrigerants have unique but overlapping condensation temperatures in the range 220–290 K. The temperature of the copper tubing is regulated by modulating the drive voltage through two thermoelectric modules which are located at each end of the copper core tube. The drive voltage is controlled by a proportional-integral-derivative signal (PID) servo loop. The hot side of each thermoelectric module is in contact with a small-plate-type heat exchanger/evaporator which is fed by a long capillary tube containing the refrigerant mixture.

We observed that depending on the setpoint temperature change ΔT_s , the cooling rate varies from 16 mK/min at $\Delta T_s = 20$ K to 40 mK/min at $\Delta T_s = 40$ K. We found no evidence of thermal-induced misalignment of the ring-down mirrors for cooling rates in the range. For $\Delta T_s = 20$ K, the ring-down cell typically can achieve a temperature stability of ± 2 mK (over a period of about 4 h) within 20 h of changing the setpoint temperature. After more than 24 h, the cell temperature exhibits an improved temperature stability of

± 0.2 mK and the maximum axial temperature difference is less than 50 mK. The cooling system also enables control of the temperature gradient along the axis of refrigerated enclosure. This capability makes it possible to adjust the temperature difference between the two ends of the copper tubing over the range ± 2 K, thereby compensating for axial gradients caused by spatial differences in heat loading.

A vacuum envelope surrounding the copper surface bounding the invar ring-down cell acts as an effective insulator to radial heat transfer. However, because the ends of the enclosure are open to the atmosphere, axial conduction from the surroundings to the cell is the dominant mode of heat transfer. To minimize this unwanted heat load, we insert cylindrical insulating foam plugs (10-cm long) into each end. We found that these plugs were essential to achieving good temperature stability.

At low temperatures, dew or frost formed by condensation of ambient humidity can deposit on the windows of the invar cell. To avoid this problem, a gentle flow of dry

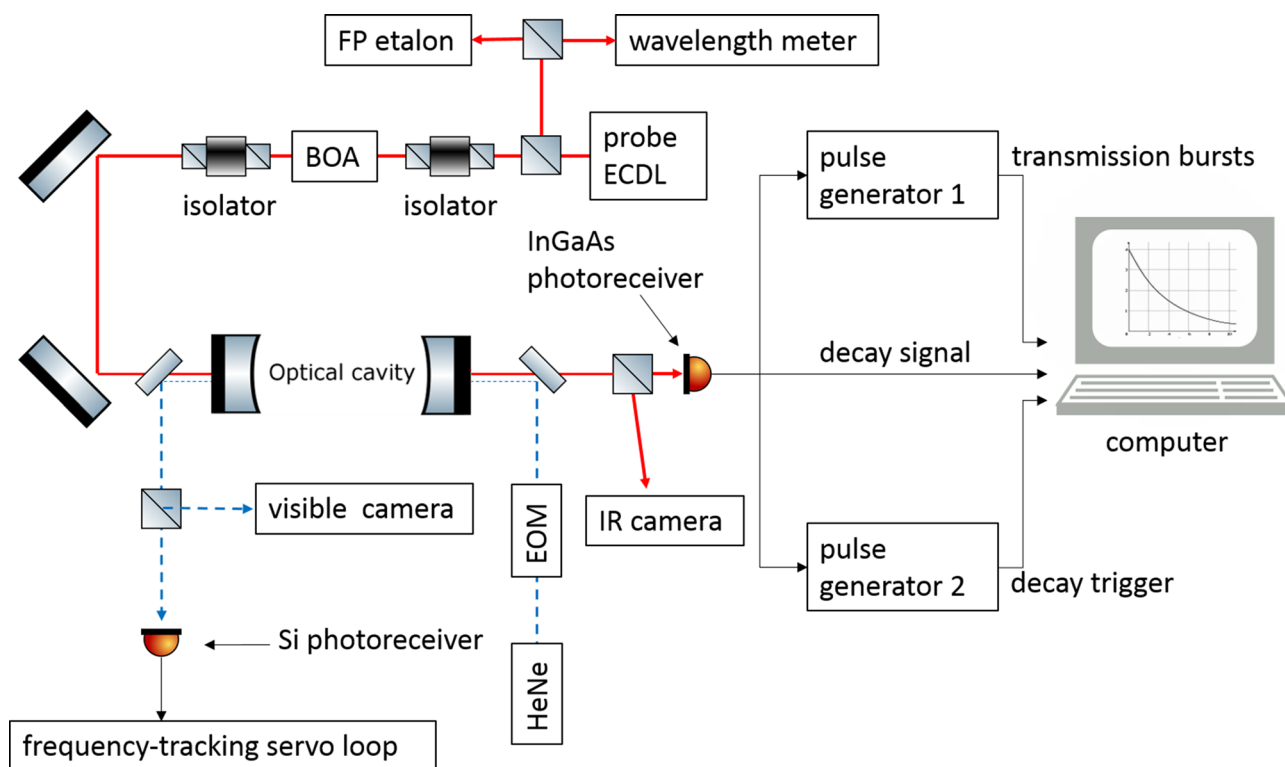


Fig. 3 Optoelectronic layout of the cavity ring-down spectroscopy system. External cavity diode laser (ECDL), booster optical amplifier (BOA), electro-optic phase modulator (EOM), Fabry-Pérot (FP)

nitrogen is permanently maintained at the outer surface of each window. This purge gas flows inside a 3-mm OD stainless steel tube that is welded onto the second set of flanges (purge gas inlets in Fig. 2 and dry-nitrogen inlet in Fig. 1a).

2.3 Optical configuration and measurement statistics

The optical system for the CRDS measurements uses a single-mode, fiber-coupled, external-cavity diode laser (ECDL) beam, 60 dB of isolation, a fiber-coupled booster-optical amplifier (BOA) used for switching off the laser power to initiate the decay events, free-space mode-matching optics and a scanning Fabry-Pérot etalon which measures the laser detuning to guide the mode-by-mode jumping. We quantified the switching response speed of the BOA and current driver (1 MHz of modulation-bandwidth) combination, and found fall times of approximately 0.3 μ s and extinction ratios exceeding 70 dB. The transmitted signal is measured with a 10 MHz bandwidth, adjustable-gain InGaAs photoreceiver and is digitized using a 16-bit, DC coupled A/D board at a sampling rate of 200 Msamples/s. The decay time τ_0 of the empty-cavity is 75 μ s, yielding an intensity reflectivity $R=0.999965$ and base loss

per-unit-length $\alpha_0 = 1/(c\tau_0) = (1 - R)/L = 4.4 \times 10^{-7} \text{ cm}^{-1}$ where c is the speed of light. See Fig. 3 for a schematic diagram of the optical layout, photonics and electronics components.

We achieve single-mode excitation of the cavity and eliminate laser drift by dithering the laser frequency through a range of 1 MHz and by maximizing the rate of transmission bursts through the cavity as described in Ref [5]. Once the laser frequency is locked to a cavity mode, the BOA is switched off at a constant trigger level, thereby initiating decay events of constant amplitude. The single-mode excitation of the cavity results in exponential decays, which are fit with three parameters: decay amplitude, decay time and constant offset. Typically, about 200 decays are acquired and individually fit to yield the average and standard deviation of the decay time. The relative standard deviation of the fitted decay times typically ranges from 0.02% to 0.04%. Using the laser frequency-lock described above, we obtain ring-down signal acquisition rates of approximately 10 Hz. We have recently modified the spectrometer to use a high-bandwidth wavelength meter for mode-by-mode locking of the probe laser to the ring-down cavity as an alternative to the Fabry-Pérot etalon/transmission lock implemented in this article. With this method, see Lin et al.

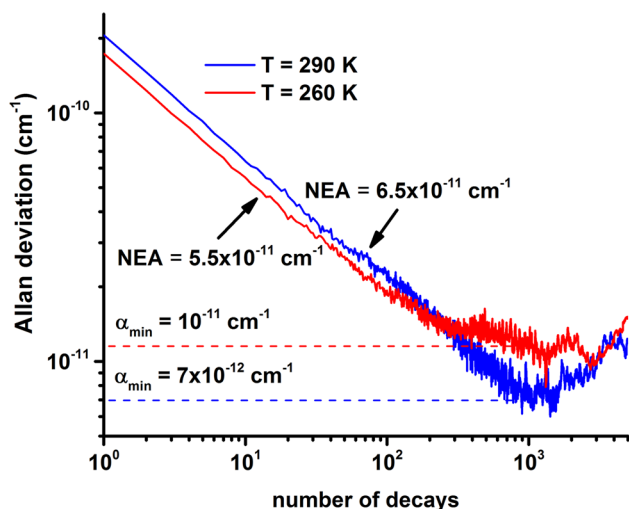


Fig. 4 Allan deviation of empty-cavity losses at the indicated setpoint temperatures. Both data sets exhibit noise-equivalent-absorption coefficients of approximately $6 \times 10^{-11} \text{ cm}^{-1} \text{ Hz}^{-1/2}$ based on a ring-down signal acquisition rate of 10 Hz

[16], ring-down signal acquisition rates are approximately 250 Hz, and 45-GHz-wide spectral scans take approximately 30 min to complete.

The Allan deviation provides a useful measure of the long-term statistical behavior of the measured decay times. Figure 4 shows a pair of Allan deviations in dimensions of loss-per-unit-length, acquired at setpoint temperatures of 260 K and 290 K, respectively. These Allan deviations have similar minimum detectable absorption coefficients of $1 \times 10^{-11} \text{ cm}^{-1}$ and $7 \times 10^{-12} \text{ cm}^{-1}$ at 260 K and 290 K, respectively. We do not consider this difference to be significant given that variations of this magnitude can occur because of slight changes in laser throughput and signal-to-noise ratio of the decay signals. Both minima occur for averaging times of approximately 100 s (1000 decays). These results also illustrate that the measurement statistics for this CRDS system are not strongly dependent on the setpoint temperature.

3 Characterization of the ring-down cavity frequency axis

3.1 Model for the temperature and pressure dependence of the cavity resonances

An optical cavity formed by two low-loss mirrors that are separated by a distance L , sustains multiple resonant frequencies associated with different longitudinal and transverse modes. For a given transverse mode, the

longitudinal modes are separated by the free spectral range (FSR) given by,

$$\nu_F = \frac{c}{2n_r L}, \quad (1)$$

in which n_r is the real part of the sample refractive index, which depends on gas composition, optical frequency ν , temperature T and pressure p . Considering only the lowest-order transverse mode TEM_{00} , then the frequency of the longitudinal mode order q is

$$\nu_q = \nu_F(q + \theta) = \frac{c}{2n_r L}(q + \theta), \quad (2)$$

where the quantity θ represents the phase-shift-per-reflection from each mirror, which can be treated as constant over narrow wavelength intervals. For simplicity, we omit this phase shift term below.

Changes in the cavity temperature affect the cavity length and, therefore, alter the FSR and shift the resonance frequencies. As discussed below, this effect can be modeled in terms of the thermal expansion coefficient of the mechanical structure to which the ring-down cavity mirrors are attached, and it can be observed by measuring the FSR under vacuum conditions (empty-cavity case) where n_r is unity. Differentiating Eq. 2 with respect to L , and defining the effective thermal expansion coefficient of the mechanical assembly as $\beta(T) = d \ln(L)/dT$, gives the derivative of the mode frequency with respect to temperature as:

$$\frac{d\nu_q}{dT} = -\beta(T)\nu_q. \quad (3)$$

As described above, the ring-down cavity in this study consists of an 80-cm-long tube (composed of invar-36) with two 4-mm thick BK7 mirrors (glued to stainless steel flanges) which are mounted near the end plane of the tube. Invar-36 has a thermal expansion coefficient exhibiting a slow variation over the temperature interval 220–290 K which can be approximated by the linear relation $\beta = \beta_0 + \frac{d\beta}{dT}(T - T_0)$, where $\beta_0 = 1.08 \times 10^{-6} \text{ K}^{-1}$, $d\beta/dT = -1.17 \times 10^{-8} \text{ K}^{-2}$ and $T_0 = 290 \text{ K}$ ([http://cryogenics.nist.gov/MPropsMAY/Invar\(Fe-36Ni\)/Invar_rev.htm](http://cryogenics.nist.gov/MPropsMAY/Invar(Fe-36Ni)/Invar_rev.htm)). In addition, the thermal expansion of the two mirrors ($\beta = 7.1 \times 10^{-6} \text{ K}^{-1}$) tends to reduce the cavity length. Given that the ratio of mirror length to invar tube length is small, we estimate that the composite (tube plus mirrors) thermal expansion coefficient is approximately 7% smaller than that of the invar-36. Integrating Eq. 3 and assuming small changes in the ring-down cavity length then,

$$\nu_q = q\nu_{F,0} \left[1 - \beta_0(T - T_0) - \frac{1}{2} \frac{d\beta}{dT}(T - T_0)^2 \right], \quad (4)$$

where $\nu_{F,0}$ is the empty-cavity FSR value at temperature T_0 , q is the longitudinal mode order and the thermal expansion coefficient terms represent those of the composite (tube plus mirrors) system.

The FSR also depends on refractive index n_r , which in turn varies with sample temperature, T and pressure p . Ciddor [25] gives detailed expressions for the pressure, temperature, composition and wavelength dependence of the refractive index of air, which we evaluated using the NIST Engineering Metrology Toolbox (<http://emtoolbox.nist.gov/Wavelength/Ciddor.asp>). We found that at fixed composition and wavelength, $n_r - 1$ correlates with gas density and can be approximated by:

$$n_r(T, p) - 1 = [n_r(T_0, p_0) - 1] \frac{(p/T)}{(p_0/T_0)}, \tag{5}$$

in which p_0 and T_0 are arbitrary reference values of pressure and temperature. By combining the thermal expansion and refractive index effects, the resonance frequency of mode order q and the FSR are,

$$\nu_q(T, p) = q\nu_{F,0} \frac{[1 - \beta_0(T - T_0) - \frac{1}{2} \frac{d\beta}{dT}(T - T_0)^2]}{1 + [n_r(T_0, p_0) - 1] \frac{(p/T)}{(p_0/T_0)}} = q\nu_F(T, P). \tag{6}$$

Thus as the temperature of the empty-cavity changes, the mode frequency and FSR change by an amount depending on the temperature change, the thermal expansion coefficient of the ring-down cavity, and the absolute mode frequency. For the gas-filled cavity, we assume that pressure-induced length changes in the mechanical structure are negligible. In this case, temperature affects the resonator length through thermal expansion, and changes in gas density (proportional to p/T) alter the optical pathlength and resonant frequencies through the refractive index of the medium.

3.2 Measurement of the empty-cavity free-spectral range

To determine the ring-down cavity FSR and to verify the preceding estimate of thermal expansion, we measured the empty-cavity FSR as a function of temperature. In this case, the system was evacuated and the cavity resonances were probed using a distributed-feedback (DFB) diode laser having a linewidth of ≈ 1 MHz. The DFB laser frequency was tuned stepwise from mode-to-mode through several thousand successive mode orders Δq , while measuring the laser frequency detuning at each point using a wavelength meter with a precision of ± 30 MHz. This method for determining the FSR has been discussed previously [26], and in the present case yields a standard uncertainty of 30 kHz at each temperature condition.

Here we have neglected the effects of mirror dispersion on the FSR. In Fig. 5 we show the results for four FSR measurements (solid circles) taken between 240 K and 290 K. The dashed line (calculated from Eq. 6 and the composite thermal expansion coefficient of invar-36 and the BK7 mirrors) exhibits an increase of less than 20 kHz with decreasing temperature, and a least-squares analysis yields a value of $\nu_{F,0}(T_0) = 186.718$ (8) MHz for the empty-cavity FSR. Although the measurement uncertainties are relatively large compared to the small effect being investigated, the results are consistent with the magnitude and direction of the predicted change in FSR.

3.3 Modeling of the free-spectral range as a function of temperature and pressure

Figure 5 also shows the calculated change in the cavity free-spectral range with gas temperature and pressure. These results are based on Eq. 6 and the refractive index of dry air assuming a CO_2 molar fraction of 400 $\mu\text{mol/mol}$. Parameters used in this calculation included: $T_0 = 290$ K, $p_0 = 103.325$ kPa and a probe frequency $\nu = 187.07$ THz ($\lambda = 1602.54$ nm) to give $n_r(T_0, p_0) - 1 = 2.71463 \times 10^{-4}$. At constant pressure, the refractive

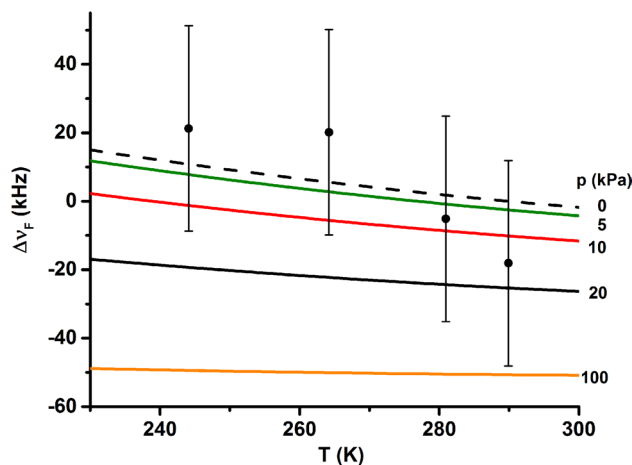


Fig. 5 Measurements (solid circles) of the change in the empty-cavity FSR relative to least-squares fit value at $T = 290$ K as a function of setpoint temperature. The error bars represent the standard uncertainty in the FSR value resulting from the fitted linear slope of wavelength meter measurement versus cavity mode order. The black dashed line corresponds to the expected change in empty-cavity FSR assuming the thermal expansion coefficient $\beta(T)$ as given in the text and using Eq. 4. The remaining lines correspond to the calculated change in the FSR (from Eq. 6) as a function of p and T that are caused by both thermal expansion of the ring-down cavity and by variation in the index of refraction of the sample gas. The refractive index calculations assume $\lambda = 1602.5$ nm and the sample to be composed of dry air with 400 $\mu\text{mol/mol}$ of CO_2

index decreases with increasing temperature, which reduces the optical pathlength and increases the FSR. This effect tends to oppose the decrease in the empty-cavity FSR (caused by thermal expansion of the invar tube) with increasing temperature. The net effect is that at a pressure of 100 kPa, the FSR is nearly independent of temperature. Over the entire range of temperature and pressure shown in Fig. 5, the maximum change in FSR relative to the empty-cavity case is approximately 65 kHz. This amount corresponds to a maximum Type B (systematic) relative uncertainty of less than 0.04% in the measured spectrum areas and widths. Although this effect is small, our analysis included the temperature- and pressure-dependent correction of the measured cavity free-spectral range.

3.4 Measurement of the absolute stability of the ring-down cavity frequency axis

The stability of the frequency axis can be precisely determined by measuring the transmission of a reference laser through the cavity. For this purpose, we constructed a closed-loop servo, in which the output of a frequency-stabilized HeNe laser ($\lambda = 633$ nm, ± 10 kHz long-term stability) was locked to a TEM₀₀ cavity resonance. This measurement exploited the reflectivity (98%) of the ring-down cavity mirrors at $\lambda = 633$ nm, resulting in transmission peaks having a full-width at half maximum of approximately 1 MHz. Prior to being mode-matched into the ring-down cavity, the HeNe beam was injected into a fiber-coupled, 10 GHz-bandwidth electro-optic phase modulator (EOM) which produced tunable sidebands symmetrically located about the optical carrier frequency. The EOM was

driven by two signals combined at a summing amplifier: a variable-frequency voltage-controlled oscillator (VCO) spanning 280 MHz to 625 MHz (used to track the shift in the cavity resonance), and a fixed-frequency sinusoid at 2 kHz with an optical modulation depth of 8 MHz (used to find the center of the cavity resonance). A first-order sideband was coupled through the ring-down cavity and monitored in transmission using a Si-PIN photoreceiver, while the optical carrier and all other sidebands were efficiently rejected by the ring-down cavity.

A schematic diagram of the servo loop is given in Fig. 6. The 2 kHz component of the signal from the photoreceiver was demodulated using a phase-sensitive amplifier. This approach yielded an error signal proportional to the derivative of a Lorentzian-profile cavity resonance with a zero-crossing for frequency discrimination. The error signal was digitized by a data-acquisition card and processed using a PID algorithm which generated an analog feedback signal through a digital-to-analog channel. With the servo loop closed, the output of the PID loop was fed back to the VCO/amplifier system to control the EOM driving frequency, thus maintaining maximum transmission of the frequency-shifted reference laser through the ring-down cavity. Changes in the output frequency of the VCO (which equal the shift in the absolute frequency of the cavity mode being interrogated) were continuously monitored with a frequency counter.

Figure 7a shows the EOM modulation frequency monitored over a time interval of approximately 40 h at a set-point temperature of 290 K. During the time to record a 45-GHz wide scan (30 min), we see frequency changes in the HeNe laser ranging from approximately 5 kHz to 550 kHz. Assuming a thermal expansion coefficient $\beta_0 =$

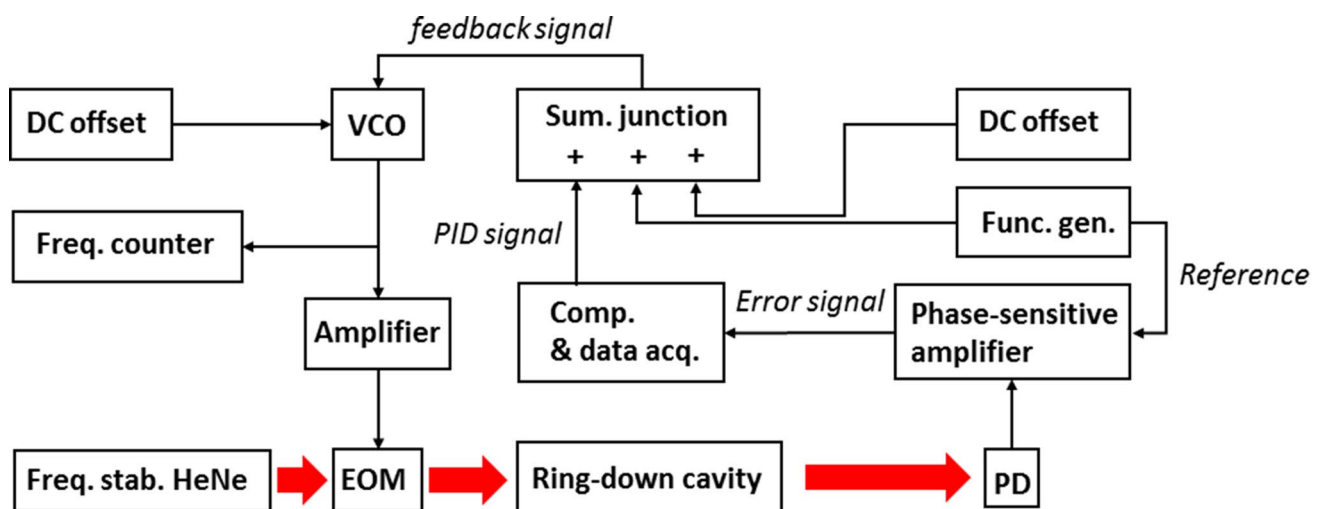


Fig. 6 Schematic of frequency-tracking servo system used to measure the frequency variation of the ring-down cavity resonances. Fiber-coupled electro-optic phase modulator (EOM), voltage-controlled

oscillator (VCO), proportional-integral derivative algorithm (PID) and feedback signal. *Thick red arrows* indicate the HeNe laser beam, and the remaining *arrows* indicate analog electronic signals

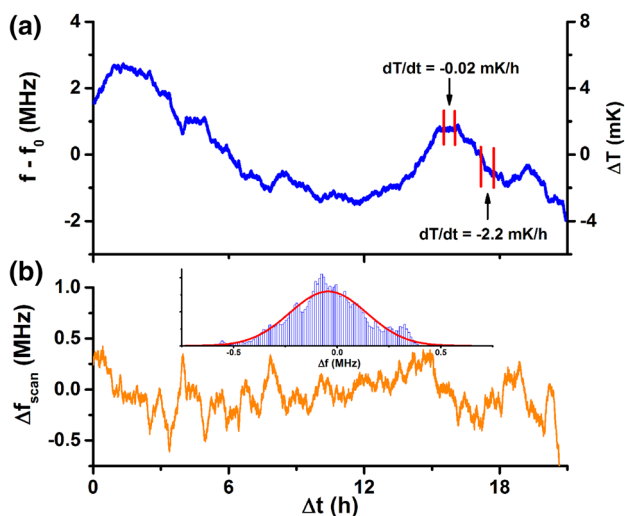


Fig. 7 **a** Variation ($f - f_0$) in the cavity resonance frequency measured with the frequency-tracking servo illustrated in Fig. 6. The cavity resonance was interrogated with a frequency-stabilized HeNe laser ($\lambda = 633$ nm) having a long-term stability of ± 10 kHz. The y-axis on the right side is the calculated temperature change assuming $(T) = 1 \times 10^{-6} \text{ K}^{-1}$. Two windows (vertical dashed lines) are indicated which represent the minimum and maximum excursions observed during a 30-min spectrum-acquisition time interval. The indicated temperature derivatives correspond to linear fits of $\Delta T(t)$ over these two time intervals. Setpoint temperature = 290 K, $f_0 = 382.923$ MHz. **b** The corresponding average frequency shift over a 30-min time interval. The inset is a histogram of the measured frequency shifts (columns) and fitted normal distribution (solid curve). The fitted mean value and standard deviation are -44 and 186 kHz, respectively

$1 \times 10^{-6} \text{ K}^{-1}$, the corresponding maximum temperature change is estimated to be nominally 1 mK. Further, we note that the range of frequency shifts at the probe laser wavelength are smaller by the wavelength-ratio factor ($633 \text{ nm}/1602.5 \text{ nm}$) and are nominally less than 200 kHz. Thus, we estimate $\Delta \nu_q = 200$ kHz to be an upper bound for concurrent cavity mode shifts (relative to the assumed equidistant mode spacing) in the absorption spectra reported here. In a more detailed statistical analysis of the data plotted in Fig. 7a, we also calculated the average frequency shift Δf of the cavity mode at $\lambda = 633$ nm as a function of time for a sliding set of 30-min-long time windows. As shown in Fig. 7b, this analysis reduces to a quasi-random distribution of positive and negative frequency shifts-per-scan with a mean value of -44 kHz. Fitting a normal distribution to the generated histogram (inset of Fig. 7b) gives a standard deviation in Δf equal to 186 kHz. Based on this result, temperature variations over a 30-min time interval contribute a Type A (random) standard uncertainty of approximately 70 kHz (corresponding to $\Delta f = 186$ kHz multiplied by the wavelength-ratio factor mentioned above), to the detuning axis of the absorption spectra.

We also carried out another set of cavity stability measurements at a temperature of 260 K, although we used another HeNe laser specified to have long-term frequency variation of ± 500 kHz. Over a time interval of 30 min, we found that the maximum frequency excursion was approximately 1 MHz consistent with the reference laser stability, thus ruling out significant degradation of the the ring-down cavity frequency stability at this lower-temperature condition.

4 Models for data analysis

4.1 Transforming measured decay rates to absorption spectra

The total loss-per-unit length of the ring-down cavity containing an absorbing sample equals the sum of the base losses associated with the high-reflectivity mirrors α_0 , the frequency-dependent absorption coefficient of the sample $\alpha_{ab}(\Delta \nu_q)$, and any weak and slowly varying losses such as Rayleigh scattering which we neglect. However, because of coupled-cavity effects, the base losses can exhibit multiple sinusoidal oscillations in frequency about a mean value $\bar{\alpha}_0$, which we denote by $\alpha_{et}(\Delta \nu_q)$. With these definitions, for data reduction, we modeled the decay signals at each frequency step as

$$\frac{1}{c\tau(\Delta \nu_q)} = \bar{\alpha}_0 + \alpha_{et}(\Delta \nu_q) + \alpha_{ab}(\Delta \nu_q), \tag{7}$$

in which the left-hand-side is a measured quantity and $\Delta \nu_q = \nu_F(T, p)\Delta q$ is the spectrum detuning. Typically two etalons are observed which are associated with the window-to-ring-down mirror distance and/or the ring-down mirror thickness, respectively. These can be characterized by Fourier analysis of empty-cavity spectra to yield characteristic periods and amplitudes. These etalon features are subtracted from the absorption spectra by floating the respective phases. After baseline subtraction, the absorption coefficient of the absorption transition is

$$\alpha_{ab}(\Delta \nu_q) = S(T)g(\nu_{q0} + \Delta \nu_q - \nu_i) \frac{x_{ab}P}{k_B T}, \tag{8}$$

where S , g and ν_i represent the intensity, line profile and absolute line position, respectively, ν_{q0} is the absolute frequency corresponding to the first spectrum point $\Delta q = 0$, x_{ab} is the molar fraction of the absorber, and k_B is the Boltzmann constant.

4.2 Line shape models

As presented below, we analyzed the measured spectra using two line profiles: the speed-dependent Voigt profile

(SDVP) and the speed-dependent Nelkin-Ghatak profile (SDNGP), which is often referred to as Rautian profile. Both profiles were used in previous studies of the same CO₂ transition. A more comprehensive line shape study covering additional profiles and numerous lines in the (30013-00001) band of ¹²C¹⁶O₂ will be published in a separate paper. Here we give only a brief description of these two speed dependent profiles used here. For more details, we refer the reader to previous publications [27–29].

The SDVP generalizes the commonly used Voigt profile (VP) to incorporate the effects of speed dependence of the collisional broadening and shifting terms. Fitted line parameters include: Doppler halfwidth, velocity-averaged Lorentzian halfwidth, speed dependent relaxation rate, velocity-averaged line shift, and speed-dependent line shift given by $(\Gamma_D, \Gamma_0, \Gamma_2, \Delta_0, \Delta_2)$, respectively. The SDNGP [30–32] generalizes the SDVP by including the effects of velocity-changing collisions under the hard-collision approximation. These types of collisions tend to reduce the Doppler broadening, which leads to Dicke (collisional) narrowing. The magnitude of the Dicke narrowing effect is captured in a sixth fitted line parameter: frequency of velocity-changing-collisions ν_{vc} . With the exception of the Doppler width, which depends on temperature, absorber mass and transition frequency, the other line profile parameters $(\Gamma_0, \Gamma_2, \Delta_0, \Delta_2, \nu_{vc})$ are proportional to pressure and depend on temperature. For both profiles we make the quadratic approximation for speed dependence of line broadening and shift [30, 31, 33]. With this assumption, the reduced speed-dependent width function $B_w(x)$ and reduced shift function $B_s(x)$ used in the velocity-averaging integration [29] are

$$B_w(x) = 1 + \frac{\Gamma_2}{\Gamma_0}(x^2 - 3/2) = 1 + a_w(x^2 - 3/2), \quad (9)$$

and

$$B_s(x) = 1 + \frac{\Delta_2}{\Delta_0}(x^2 - 3/2) = 1 + a_s(x^2 - 3/2), \quad (10)$$

in which x is the reduced collision velocity, and where the dimensionless broadening and shifting speed-dependence parameters are defined as $a_w = \Gamma_2/\Gamma_0$ and $a_s = \Delta_2/\Delta_0$. Note that a_w and a_s are expected to be independent of pressure. We also point out that the quadratic version of the SDNGP is a limiting case of the so-called Hartmann-Tran profile (HTP) [34, 35], which corresponds to a correlation parameter $\eta = 0$.

The following derivation shows that under the quadratic approximation and assuming a power-law temperature dependence for the pressure broadening coefficient $\gamma_0(T)$, a_w is independent of temperature with a magnitude that is a simple function of the temperature exponent n and perturber-to-absorber mass ratio m_p/m_a .

At fixed gas density, Eq. 12 of Lisak et al. [36] gives

$$\Gamma_2(T) = \frac{2}{3} \frac{m_p/m_a}{1 + m_p/m_a} T \frac{d\Gamma_0(T)}{dT}. \quad (11)$$

Given a power-law temperature dependence of the form $\gamma_0(T) = \gamma_0(T_r)(T_r/T)^n$ where T_r is a reference temperature (typically 296 K), we can write the Lorentzian halfwidth as,

$$\Gamma_0(T) = \left(\frac{T_r}{T}\right)^n \gamma_0(T_r) p = \left(\frac{T_r}{T}\right)^n \gamma_0(T_r) N k_B T \quad (12)$$

where N is the ideal gas number density and $\gamma_0(T_r)$ is the pressure broadening coefficient at the reference temperature. After substitution of Eq. 12 in Eq. 11, followed by differentiation and rearrangement, we obtain

$$a_w = \frac{\Gamma_2}{\Gamma_0} = (1 - n) \frac{2}{3} \frac{m_p/m_a}{1 + m_p/m_a}, \quad (13)$$

which is fully consistent with Eq. 20 of Lisak et al. [36], recognizing that their value of $n/2$ is equivalent to $1 - n$ given here. This result shows that the normalized speed-dependent broadening parameter ratio ($a_w = \Gamma_2/\Gamma_0$) is theoretically independent of temperature as well as pressure, which is a relation that may be used to constrain multispectrum global fits that cover a wide range of gas conditions.

5 Measurement results

As an illustration of the present system performance for high-accuracy line shape analysis, we probed the air-broadened (30013-00001) band R16e transition of ¹²C¹⁶O₂ at $\tilde{\nu} = 6240.1045$ cm⁻¹. The band to which this transition belongs is the weaker of the two carbon dioxide bands used in the GOSAT, OCO-2 and TCCON missions. Although this band has been extensively studied at room temperature [37–52], only a few low-temperature studies have been reported [53–55].

Measurements were made over the temperature range 240–290 K and for each temperature spectra at multiple pressures (5, 9, 13, 21, 43 and 59) kPa were recorded. All samples consisted of static charges consisting of nominally 400 μmol mol⁻¹ of CO₂ in purified, dry air.

At a fixed setpoint temperature, the SDVP and SDNGP were fit using a multispectrum Levenberg-Marquard least-squares fitting program to spectra acquired over the pressure range listed above. In the fitting procedure, we used the theoretical value for the Doppler width and we constrained Γ_0 and ν_{vc} (in the case of the SDNGP) to be proportional to pressure. The pressure-induced shifting term Δ_0 was set to 0, because absolute line positions were not

measured. This constraint also precluded determination of Δ_2 , which is also difficult to retrieve from the line profile fits because of its relatively small magnitude. Other floated parameters included the line center, peak area and a_w . As a representative example of the system performance, Fig. 8 shows the measurements (symbols), SDNGP fit (line, upper panel) and SDVP and SDNGP residuals (lower panels) for a single spectrum measured at $(T, p) = (280 \text{ K}, 13.4 \text{ kPa})$. These data exhibit a signal-to-noise ratio (SNR), defined as the ratio of peak absorption to root-mean-square baseline residual, of 20,000:1. Another figure-of-merit, the quality-of-fit (QF) factor (as defined by Cygan et al. [14]) generally is less than or equal to the SNR and equals the ratio of peak absorption to the magnitude of fit residuals which include the systematic contributions near line center. At sufficiently high SNR, the QF is sensitive to the choice of line profile, with increasing values indicating better agreement between theory and experiment. The QF values for the SDVP and SDNGP shown in Fig. 8 are 7670 and 13,800, respectively.

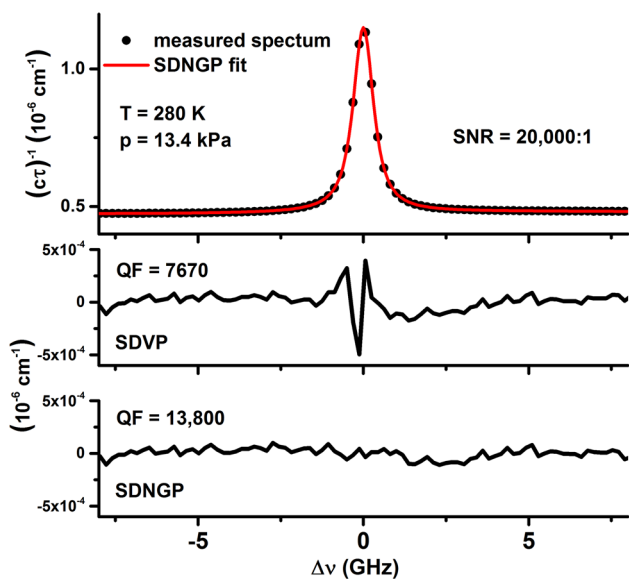


Fig. 8 Upper panel Measured spectrum (solid circles) and fit of SDNGP (solid line) at $T=280 \text{ K}$ and $p=13.4 \text{ kPa}$, for the R16e (30013-00001) $^{12}\text{C}^{16}\text{O}_2$ transition. Bottom panels Fit residuals (obs.-calc.) and quality-of-fit parameter (QF) corresponding to the SDVP and SDNGP models, respectively

Table 1 Comparison of measured line shape parameters for two R16e $^{12}\text{C}^{16}\text{O}_2$ transitions based on fits of the SDNGP to CRDS spectra

Parameter	SDNGP, this work	[16]	[56]	Rel. Diff [16]	Rel. Diff [56]
γ_{air} (kHz/Pa)	22.013 ± 0.059	22.048 ± 0.022	22.040 ± 0.020	0.16%	0.12%
n_{air}	0.6736 ± 0.0180				
a_w	0.0835 ± 0.0012	0.0883 ± 0.0002	0.0884 ± 0.0001	5.43%	5.54%

The present study is for the (30013-00001) band at variable temperature; Refs. [16, 56] are for the (30012-00001) band at room temperature. The reported standard uncertainties for this work are based on values returned by the fitting algorithm. γ_{air} is specified at $T_r = 296 \text{ K}$ and can be converted to conventional units using the identity $1 \text{ cm}^{-1} \text{ atm}^{-1} = 295.872 \text{ kHz Pa}^{-1}$

This difference in QF for these two cases is consistent with the prominent W-shaped structure about line center which is only manifest in the SDVP fit. Having an extra parameter, the SDNGP gives a QF value that is nearly twice that of the SDVP and which is 30% lower than the SNR value. This example illustrates the capability of the present CRDS system to distinguish subtle differences in theoretical line profiles and to provide high-precision determinations of line shape parameters.

Fitting the spectra with the SDNGP allowed us to compare our measurements of the air-broadening coefficient $\gamma_{\text{air}} = \Gamma_0/p$ and the a_w parameters with our previous room-temperature FS-CRDS measurements of the air-broadened (30012-00001) band R16e $^{12}\text{C}^{16}\text{O}_2$ transition [16, 56]. These previous measurements correspond to another vibrational band having the same vibrational quanta (differing only in the Fermi interaction term) and the same lower-state rotational quantum number J . Table 1 summarizes the comparison of the present fitted line shape parameters and the previously reported results. All three measured air-broadening coefficients agree to within 0.2%, although the present a_w parameter is about 5.5% lower than both literature values. Of the three parameters reported in Table 1, the air-broadening coefficient is the most precisely determined quantity (0.3% fit-based relative uncertainty), whereas the temperature exponent n has the largest relative uncertainty of 2.7% and that of a_w is 1.4%.

Evaluating $m_p/m_a = 0.658$ for the CO_2 -air system and using our measured temperature exponent $n=0.6736$, Eq. 13 gives $a_w=0.0864$. This theoretical value for a_w is within 3.4% of the present measured value of 0.0835 and within 2.4% of the measured values given in Refs. [16, 56].

The same spectra discussed above were also fit with the SDVP which enabled direct comparison with the Fourier-transform spectroscopy (FTS) measurements reported by Predoi-Cross et al. [53] and Devi et al. [54]. These studies provided the temperature dependence of the air-broadening and shift parameters for the same transition measured in the present study. The results are summarized in Table 2. We find excellent agreement with the parameters of Devi et al. [54], where absolute relative differences between γ_{air} and n are less than approximately 0.06% for both the

Table 2 Comparison of measured line shape parameters for the R16e $^{12}\text{C}^{16}\text{O}_2$ transition based on fits of the SDVP to variable-temperature FTS spectra Ref. [53, 54]

Parameter	SDVP This work	[53]	[54]	Rel. Diff [53] (%)	Rel. Diff [54] (%)
γ_{air} (kHz/Pa)	22.072 ± 0.030	22.190 ± 0.016	22.063 ± 0.010	0.5	-0.04
n_{air}	0.7160 ± 0.0132	0.673 ± 0.005	0.7164 ± 0.002	-6.0	0.06

All studies are for the (30013-00001) band; the reported uncertainties for this work are based on values returned by the fitting algorithm. γ_{air} is specified at $T_r = 296$ K and can be converted to conventional units using the identity $1 \text{ cm}^{-1} \text{ atm}^{-1} = 295.872 \text{ kHz Pa}^{-1}$

air-broadening and the temperature exponent. Larger absolute differences, up to 6% for the temperature exponent, were found by comparison to that reported in Ref. [53].

6 Conclusions

We constructed and tested a new variable-temperature cavity ring-down spectroscopy system enabling high-fidelity line shape measurements over the temperature range 220–290 K. The system comprises a monolithic, fixed-mirror, ring-down cell which resides in a thermally stabilized, refrigerated enclosure. We showed that the cavity mode frequency stability is 100 kHz or better over time scales as long as 30 min, which compares favorably to conventional FS-CRDS systems containing PZT-actuated mirrors and closed-loop servo systems. In addition, we demonstrated a minimum detectable absorption coefficient of $7 \times 10^{-12} \text{ cm}^{-1}$ for 100-s averaging times, resulting in spectra with SNR values of 20,000:1 for near-infrared CO_2 -in-air spectra at ambient concentration levels. This CRDS apparatus offers new opportunities for low-uncertainty line shape measurements of species such as carbon dioxide, oxygen and methane, and is especially suitable for multispectrum analyses spanning temperature and pressure conditions that are relevant to atmospheric remote sensing applications.

Acknowledgements This work was supported by the NIST Greenhouse Gas Measurements and Climate Research Program and NASA Contract NNH15AZ96I (Orbiting Carbon Observatory-2 Science Team). We also thank Dr. Piotr Wcisło, University of Nicolas Copernicus, Toruń Poland regarding the derivation of Eqs. 11 and 12.

References

- C.E. Miller, D. Crisp, P.L. DeCola, S.C. Olsen, J.T. Randerson, A.M. Michalak, A. Alkhaled, P. Rayner, D.J. Jacob, P. Suntharalingam, D.B.A. Jones, A.S. Denning, M.E. Nicholls, S.C. Doney, S. Pawson, H. Boesch, B.J. Connor, I.Y. Fung, D. O'Brien, R.J. Salawitch, S.P. Sander, B. Sen, P. Tans, G.C. Toon, P.O. Wennberg, S.C. Wofsy, Y.L. Yung, R.M. Law, *J. Geophys. Res.* **112**, D10314 (2007). doi:[10.1029/2006JD007659](https://doi.org/10.1029/2006JD007659)
- A. O'Keefe, D.A.G. Deacon, *Rev. Sci. Instrum.* **59**, 2544 (1988)
- D. Romanini, A.A. Kachanov, F. Stoeckel, *Chem. Phys. Lett.* **270**, 538 (1997)
- J. Morville, D. Romanini, A. A. Kachanov, M. Chenevier, *Appl. Phys. B* **78**, 465 (2004)
- J.T. Hodges, R. Ciuryło, *Rev. Sci. Instrum.* **76**, 023112 (2005)
- J. T. Hodges and D. Lisak, *Appl. Phys. B* **85**, 375 (2006)
- J.T. Hodges, H.P. Layer, W.W. Miller, G.E. Scace, *Rev. Sci. Instrum* **75**, 849 (2004)
- D. A. Long, M. Okumura, C. E. Miller, J. T. Hodges, *Appl. Phys. B* **105**, 471 (2011)
- D.A. Long, A. Cygan, R.D. van Zee, M. Okumura, C.E. Miller, D. Lisak, J.T. Hodges, *Chem. Phys. Lett.* **536**, 1 (2012)
- D.A. Long, D.J. Robichaud, J.T. Hodges, *J. Chem. Phys.* **137**, 014307 (2012)
- G.-W. Truong, K. O. Douglass, S. E. Maxwell, R. D. van Zee, D.F. Plusquellic, J.T. Hodges, D.A. Long, *Nat. Photon.* **7**, 532 (2013)
- D.A. Long, G.-W. Truong, R. D. van Zee, D.F. Plusquellic, J.T. Hodges, *Appl. Phys. B* **114**, 489 (2013)
- S. Kassi, A. Campargue, *J. Chem. Phys.* **137**, 234201 (2012)
- A. Cygan, D. Lisak, S. Wójtewicz, J. Domysławska, J.T. Hodges, R.S. Trawiński, R. Ciuryło, *Phys. Rev. A* **85**, 022508 (2012)
- V.T. Sironneau, J.T. Hodges, *J. Quant. Spectrosc. Radiat. Transf.* **152**, 1 (2015)
- H. Lin, Z.D. Reed, V.T. Sironneau, J.T. Hodges, *J. Quant. Spectrosc. Radiat. Transf.* **161**, 11 (2015)
- T. Delahaye, S.E. Maxwell, Z.D. Reed, H. Lin, J.T. Hodges, K. Sung, V.M. Devi, T. Warneke, P. Spietz, H. Tran, *J. Geophys. Res. Atmos* **121**, 2016JD025024 (2016)
- Y. Perez-Delgado, C.E. Manzanares, *Appl. Phys. B* **106**, 971 (2011)
- Y. Perez-Delgado, C.E. Manzanares, *J. Phys. Chem. A* **114**, 7918 (2010)
- Y. Perez-Delgado, E.K. Lewis, C.J. Moehnke, M.C. Salazar, A.J. Hernandez, C.E. Manzanares, *Mol. Phys* **107**, 1367 (2009)
- E.K. Lewis, C.J. Moehnke, J.G. Navea, C.E. Manzanares, *Rev. Sci. Instrum* **77**, 073107 (2006)
- C.J. Moehnke, E.K. Lewis, A. Lopez-Calvo, C.E. Manzanares, *Chem. Phys. Lett.* **418**, 576 (2006)
- J. Morville, D. Romanini, A. Campargue, R. Bacis, *Chem. Phys. Lett.* **363**, 498 (2002)
- S. Kassi, D. Romanini, A. Campargue, *Chem. Phys. Lett.* **477**, 17 (2009)
- P. E. Ciddor, *Appl. Opt.* **35**, 1566 (1996).
- D.J. Robichaud, J.T. Hodges, P. Masłowski, L.Y. Yeung, M. Okumura, C.E. Miller, L.R. Brown, *J. Mol. Spectrosc.* **251**, 27 (2008)
- P.R. Berman, *J. Quant. Spectrosc. Radiat. Transf.* **12**, 1331 (1972)
- S.G. Rautian, I.I. Sobel'man, *Sov. Phys. Uspekhi* **9**, 701 (1967)
- R. Ciuryło, *Phys. Rev. A* **58**, 1029 (1998)
- F. Rohart, H. Mäder, H.-W. Nicolaisen, *J. Chem. Phys.* **101**, 6475 (1994)

31. F. Rohart, A. Ellendt, F. Kaghat, H. Mäder, J. Mol. Spectrosc. **185**, 222 (1997)
32. B. Lance, G. Blanquet, J. Walrand, J.-P. Bouanich, J. Mol. Spectrosc. **185**, 262 (1997)
33. A.S. Pine, R. Ciurylo, J. Mol. Spectrosc. **208**, 180 (2001)
34. N. H. Ngo, D. Lisak, H. Tran, J.-M. Hartmann, J. Quant. Spectrosc. Radiat. Transf. **129**, 89 (2013)
35. J. Tennyson, P.F. Bernath, A. Campargue, A.G. Csaszar, L. Daumont, R.R. Gamache, J.T. Hodges, D. Lisak, O.V. Naumenko, L.S. Rothman, H. Tran, N.F. Zobov, J. Buldyreva, C.D. Boone, M.D. De Vizia, L. Gianfrani, J.-M. Hartmann, R. McPheat, J. Murray, N.H. Ngo, O.L. Polyansky, D. Weidmann, Recommended isolated-line profile for representing high-resolution spectroscopic transitions (IUPAC Technical Report). Pure Appl. Chem. **86**, 1931 (2014)
36. D. Lisak, A. Cygan, P. Wcisło, R. Ciuryło, J. Quant. Spectrosc. Radiat. Transf. **151**, 43 (2015)
37. L. Régalia-Jarlot, V. Zéninari, B. Parvitte, A. Grossel, X. Thomas, P. von der Heyden, G. Durry, J. Quant. Spectrosc. Radiat. Transf. **101**, 325 (2006)
38. R.A. Toth, L.R. Brown, C.E. Miller, V.M. Devi, D.C. Benner, J. Mol. Spectrosc. **239**, 221 (2006)
39. R.A. Toth, L.R. Brown, C.E. Miller, V.M. Devi, D.C. Benner, J. Mol. Spectrosc. **239**, 243 (2006)
40. R.A. Toth, C.E. Miller, V. Malathy Devi, D.C. Benner, L.R. Brown, J. Mol. Spectrosc. **246**, 133 (2007)
41. R.A. Toth, C.E. Miller, L.R. Brown, V.M. Devi, D.C. Benner, J. Mol. Spectrosc. **243**, 43 (2007)
42. R.A. Toth, L.R. Brown, C.E. Miller, V. Malathy Devi, D.C. Benner, J. Quant. Spectrosc. Radiat. Transf. **109**, 906 (2008)
43. V.M. Devi, D.C. Benner, L.R. Brown, C.E. Miller, R.A. Toth, J. Mol. Spectrosc. **245**, 52 (2007)
44. V.M. Devi, D.C. Benner, L.R. Brown, C.E. Miller, R.A. Toth, J. Mol. Spectrosc. **242**, 90 (2007)
45. A. Predoi-Cross, A.V. Unni, W. Liu, I. Schofield, C. Holladay, A.R.W. McKellar, D. Hurtmans, J. Mol. Spectrosc. **245**, 34 (2007)
46. A. Predoi-Cross, W. Liu, C. Holladay, A.V. Unni, I. Schofield, A.R.W. McKellar, D. Hurtmans, J. Mol. Spectrosc. **246**, 98 (2007)
47. J.-M. Hartmann, H. Tran, G.C. Toon, Atmos. Chem. Phys. **9**, 7303 (2009)
48. D. A. Long, G.-W. Truong, J.T. Hodges, C. E. Miller, J. Quant. Spectrosc. Radiat. Transf. **130**, 112 (2013)
49. J. Lamouroux, R.R. Gamache, A.L. Laraia, J.-M. Hartmann, C. Boulet, J. Quant. Spectrosc. Radiat. Transf. **113**, 1536 (2012)
50. R. R. Gamache, J. Lamouroux, A.L. Laraia, J.-M. Hartmann, C. Boulet, J. Quant. Spectrosc. Radiat. Transf. **113**, 976 (2012)
51. C.E. Miller, L.R. Brown, J. Mol. Spectrosc. **228**, 329 (2004)
52. C.E. Miller, M.A. Montgomery, R.M. Onorato, C. Johnstone, T.P. McNicholas, B. Kovacic, L.R. Brown, J. Mol. Spectrosc. **228**, 355 (2004)
53. A. Predoi-Cross, A.R.W. McKellar, D.C. Benner, V.M. Devi, R.R. Gamache, C.E. Miller, R.A. Toth, L.R. Brown, Can. J. Phys. **87**, 517 (2009)
54. V. M. Devi, D. C. Benner, K. Sung, L. R. Brown, T. J. Crawford, C. E. Miller, B. J. Drouin, V. H. Payne, S. Yu, M. A. H. Smith, A. W. Mantz, R. R. Gamache, J. Quant. Spectrosc. Radiat. Transf. **177**, 117 (2016)
55. A. Predoi-Cross, W. Liu, R. Murphy, C. Povey, R. R. Gamache, A. L. Laraia, A. R. W. McKellar, D. R. Hurtmans, V. Malathy Devi, J. Quant. Spectrosc. Radiat. Transf. **111**, 1065 (2010)
56. D. A. Long, S. Wójtewicz, C. E. Miller, J. T. Hodges, J. Quant. Spectrosc. Radiat. Transf. **161**, 35 (2015)